Deformation-compensated averaging for clutter reduction in epiphotoacoustic imaging *in vivo*

Michael Jaeger
David Harris-Birtill
Andreas Gertsch
Elizabeth O'Flynn
Jeffrey Bamber

Deformation-compensated averaging for clutter reduction in epiphotoacoustic imaging *in vivo*

Michael Jaeger,[a,b] **David Harris-Birtill,**[a] **Andreas Gertsch,**[a] **Elizabeth O'Flynn,**[b,c] **and Jeffrey Bamber**[a,b]

[a]Institute of Cancer Research and Royal Marsden NHS Foundation Trust, Joint Department of Physics, Sutton, Surrey, SM2 5PT, United Kingdom
[b]Institute of Cancer Research and Royal Marsden NHS Foundation Trust, CRUK-EPSRC Cancer Imaging Centre, Sutton, Surrey, United Kingdom
[c]Royal Marsden NHS Foundation Trust, Radiology Department, Sutton, Surrey, United Kingdom

Abstract. Photoacoustic imaging, based on ultrasound detected after laser irradiation, is an extension to diagnostic ultrasound for imaging the vasculature, blood oxygenation and the uptake of optical contrast media with promise for cancer diagnosis. For versatile scanning, the irradiation optics is preferably combined with the acoustic probe in an epi-style arrangement avoiding acoustically dense tissue in the acoustic propagation path from tissue irradiation to acoustic detection. Unfortunately epiphotoacoustic imaging suffers from strong clutter, arising from optical absorption in tissue outside the image plane, and from acoustic backscattering. This limits the imaging depth for useful photoacoustic image contrast to typically less than one centimeter. Deformation-compensated averaging (DCA), which takes advantage of clutter decorrelation induced by palpating the tissue with the imaging probe, has previously been proposed for clutter reduction. We demonstrate for the first time that DCA results in reduced clutter in real-time freehand clinical epiphotoacoustic imaging. For this purpose, combined photoacoustic and pulse-echo imaging at 10-Hz frame rate was implemented on a commercial scanner, allowing for ultrasound-based motion tracking inherently coregistered with photoacoustic frames. Results from the forearm and the neck confirm that contrast is improved and imaging depth increased by DCA. © *2012 Society of Photo-Optical Instrumentation Engineers (SPIE).* [DOI: 10.1117/1.JBO.17.6.066007]

Keywords: optoacoustic; ultrasonography; medical imaging; contrast improvement; penetration depth; motion tracking; tissue deformation; palpation.

Paper 11785 received Dec. 22, 2011; revised manuscript received Apr. 6, 2012; accepted for publication Apr. 10, 2012; published online Jun. 4, 2012.

1 Introduction

Photoacoustic (PA) imaging shows tissue optical-absorption contrast, based on the detection of ultrasound that is thermoelastically generated after irradiation with ns-pulsed laser light.[1] When detecting the ultrasound signals with an array of transducers, a spatially resolved map of the local density of absorbed laser light can be reconstructed, using established time- or frequency-domain algorithms.[2–5] PA methods are suited for imaging the vasculature because hemoglobin is a main source of optical contrast in tissue for visible and near-infrared wavelengths. Moreover, PA imaging allows spatially-resolved measurement of the local blood oxygenation level, due to the different optical-absorption spectra of oxygenated and deoxygenated hemoglobin.[6–9] By acquiring multiple PA images, each using a different wavelength of optical irradiation, the local oxygenation level can be calculated from the wavelength-dependent signal amplitude. Similar methods may be used to image the uptake of optical contrast media that may be passive[10–13] or targeted[14,15] dyes and nanoparticles. Photoacoustic imaging therefore holds promise for the diagnosis of vascular diseases and cancer,[16,17] for assessing tumour hypoxia (for the selection and control of radiotherapy and of novel vascularization-modification treatment strategies) and for monitoring tumor response to treatment.[18,19] These and many other potential benefits provide strong motivation for the development of clinically useful PA imaging instrumentation.

For broad clinical application, PA imaging is preferably implemented as an extension to the existing clinical diagnostic ultrasound method, which is already widely used for diagnosis of vascular conditions and cancer staging and treatment monitoring. Thus it would be performed using freehand scanning, in real time, and combined with ultrasound using the same probe in a single device. In such a combined approach, the PA signal can be displayed within the anatomical context shown in pulse-echo images,[20–28] and the overall diagnostic value substantially benefits from the complementary nature of the two imaging modalities. In contrast to Doppler imaging, which is sensitive to blood flow, PA imaging does not require flow and is therefore in principle also sensitive to small blood vessels and regions of stationary blood that are not detected by ultrasound echo methods without the use of exogenous contrast agents. We maintain that laser illumination and ultrasound detection through the same tissue surface is preferred to avoid the effect of gas, bone and other obstructing tissue components in the acoustic propagation path from the irradiated tissue region to the probe.[29] We refer to this as epiphotoacoustic imaging, following the terminology of epimicroscopy. Epiphotoacoustic imaging follows the strategy already adopted in the design of the majority of modern (backscatter) medical ultrasound systems, which allow flexible imaging of many superficial and hollow parts of the human body.

The broad clinical success of PA imaging will depend on being able to image to an adequate depth. In theory, imaging

---

Address all correspondence to: Jeffrey Bamber, Institute of Cancer Research and Royal Marsden NHS Foundation Trust, Joint Department of Physics, Sutton, Surrey, SM2 5PT, United Kingdom. Tel: +44 20 8661 3343; Fax: +44 20 8661 3812; E-mail: Jeff.Bamber@icr.ac.uk.

to a depth of several centimeters is predicted to be feasible, considering solely optical attenuation and transducer sensitivity.[30] These predictions have been supported by experimental demonstrations of deep imaging of breast cancer *in vivo* in transmission mode[17] (irradiation and detection on opposite sides) and in orthogonal mode[16] (irradiation and acoustic detection at a right angle), and imaging of blood-filled vessel phantoms at a depth of 49 mm in human breast *ex vivo* in transmission mode.[31] However, both transmission and orthogonal mode are only feasible with acoustically quasi-transparent organs such as the breast, while epi-mode is required elsewhere.

Unfortunately, obtaining similar results using epiphotoacoustic imaging is difficult, because in epi-mode strong clutter limits contrast and thus imaging depth.[24,32] This clutter arises from strong PA ultrasound generated outside the image plane at the site of tissue irradiation, which propagates to the probe either directly (direct clutter) or after being scattered by acoustic inhomogeneities located within the image plane (echo clutter). In transmission mode, clutter tends to be generated at positions furthest from the ultrasonic receiver, and thus can be temporally separated from emissions of interest because they are the last to arrive. In epi-mode, however, clutter obscures the weak signals from deep structures. In our experience most tissues *in vivo*, which are well vascularized and contain many structures that will scatter the sound, produce clutter that limits clinical epiphotoacoustic imaging to depths that are typically less than about 1 cm. In particular, in our first experience of *in vivo* breast scanning using Duplex epiphotoacoustic and echo imaging, we identified echo clutter that limited further progress in clinical epiphotoacoustic imaging without a clutter-reduction method.[33]

As a promising step towards a clinically more useful imaging depth for epiphotoacoustics, clutter reduction by deformation-compensated averaging (DCA) has previously been developed, based on "palpation scanning." In DCA, a PA image sequence is acquired while tissue deformation is induced by palpating the tissue with the ultrasound probe, and each PA image is deformation compensated based on spatially resolved motion tracking in simultaneously acquired pulse-echo images.[24,32] In these papers it was demonstrated in realistic phantom experiments that such palpation scanning leads to clutter decorrelation in the deformation-compensated images, while true PA features persist, such that averaging of deformation-compensated images resulted in improved contrast and increased imaging depth. These studies were conducted with phantoms because of the low frame rate of the scanner used; clinical use of DCA requires real-time interleaved PA and pulse-echo imaging if patient motion is not to result in loss of registration between the two modalities and thus erroneous motion compensation.

Here we demonstrate for the first time that DCA reduces clutter in clinical epiphotoacoustic scans. This has been made possible by the new system referred to above,[33] which produces simultaneous photoacoustic and pulse-echo images at 10-Hz frame rate. In image sequences of both the neck and the forearm, clutter was identified and characterized investigating the local correlation of motion-compensated PA images as a function of time-lag. This analysis also permitted an evaluation of the effects of DCA based on the clutter decorrelation time constant. Moreover, DCA results are shown which demonstrate a slight loss of resolution but substantial contrast improvement for both neck and forearm scans, thus confirming the importance of clutter reduction for clinical epiphotoacoustic imaging.

2 Materials and Methods

2.1 *Method for Duplex Photoacoustic and Photoacoustic-Echo Imaging*

DCA of clinical PA scans for clutter reduction requires ultrasound motion tracking simultaneously with PA image acquisition, i.e., duplex PA and pulse-echo imaging. Unfortunately our ultrasound scanner (see below) did not permit real-time interleaved acquisition of photoacoustic and pulse-echo frames. In order to achieve duplex imaging, a special method was devised, which is described in detail elsewhere.[33] Briefly, the transmit wave for pulse-echo imaging was generated photoacoustically and thus echo ultrasound could be acquired simultaneously with PA data. This made it possible to operate the scanner in receive-only mode for continuous data acquisition, and thus for freehand clinical scanning. For each laser pulse, light that is absorbed by the tissue generates the PA signal in the usual way, whereas light backscattered from the tissue is absorbed at the probe surface, generating a plane PA transient that propagates into the tissue and acts like a pulse-echo transmit wave. Great care is typically taken to optically shield the probe, in order to avoid troublesome echoes generated by this PA transmit wave. In contrast to this, we have taken advantage of the PA transmit wave, placing a gelatine stand-off pad between the probe and the skin surface for temporal separation of PA signals and photoacoustically generated echo signals (henceforth called PA-echo). For a stand-off pad with sound speed c and thickness D, the first echoes were generated at a delay $\tau = D/c$ after the laser pulse, corresponding to the acoustic transit time through the stand-off, while PA transients from the tissue were generated at the same time as the laser pulse. PA-echo signals were thus delayed relative to the PA signals by τ, permitting PA imaging to a depth equal to D without interference of PA-echoes. Because PA signal levels from depths greater than D were much weaker than the PA-echo signals, "pure" pulse-echo data could be assumed after the first detection of echoes. Thus, after a single laser pulse, a PA image can be reconstructed from the signals arriving during the time interval τ to 2τ, and a pulse-echo image from those arriving during the interval 2τ to 4τ, both covering an imaging depth equal to D. The photoacoustic-echo image is, however, of much poorer quality than a conventional pulse-echo image because it uses an unfocused transmit wave and must therefore rely entirely on receive focusing (which is electronic in the plane of a linear array and mechanical in the orthogonal direction).

2.2 *Photoacoustic Imaging Equipment*

Commercial medical ultrasound imaging equipment (z.one™, Zonare Medical Systems Inc., USA) was used for PA and pulse-echo signal acquisition. When operated in a research mode, the z.one™ allows the parallel readout of up to 150 μs of signal on each of 64 transducer elements and thus the acquisition of a large data frame after each single laser pulse. Frame sequences of long (>1 min) duration can be stored at high frame rate on internal memory for subsequent read out, enabling acquisition of channel data for real-time sequences of freehand clinical scans. A linear-array transducer (L10-5, Zonare) was used for acoustic detection, featuring 5–10 MHz bandwidth (-3 dB) and 128 elements at 0.3 mm pitch.

For PA image generation, a Q-switched Nd:YAG laser (ELEN, Italy) was used at 1064-nm wavelength, delivering

70 mJ per pulse with a 7-ns pulse duration. A 10-Hz repetition rate was chosen for all experiments. The laser light was guided via a bifurcated fiber-optic bundle (Fibreoptic, Switzerland) through two line profile converters, one at each side of the linear probe. The output of the profile converters was projected through the gelatine standoff in front of the probe aperture to create two lines of irradiation adjacent to each other, each having 20-mm length and 5-mm width, thus irradiating a patch of 20 mm by 10 mm of the skin surface below the probe. This resulted in 35 mJ cm^{-2} radiant exposure, well below the ANSI safety limit of 1064 nm (100 mJ cm^{-2}).

A 20-mm-thick gelatine standoff was used, allowing duplex PA and PA-echo imaging to a tissue depth of 20 mm. Both PA and PA-echo images were reconstructed using frequency-domain algorithms.[5,34] Although the active (64-channel) receive aperture covered only the center half of the probe aperture, the lateral extent of the reconstructed image was chosen equal to the full aperture (38 mm). This was done so that the image would show steering angles pointing outside the active aperture of the probe on the one hand; on the other hand it would be easier to compare photoacoustic-echo images with conventional pulse-echo B-mode images obtained when the scanner was operating in its normal clinical mode.

2.3 Data Acquisition Procedure

Using an integrated probe containing the ultrasound transducer array, the gelatine standoff and the optical-fiber profile converters,[33] volunteers were scanned with freehand probe guidance. A scan always started with the acquisition of a z.one™ internal B-mode image. Then the z.one™ was remotely switched to passive mode, the laser started, and a sequence of 90 data frames (corresponding to 9 s at 10 Hz) was acquired and stored on the internal memory. While acquiring these 90 frames, the tissue was palpated with lateral reciprocating probe motion while keeping a sticky contact between the probe and the skin surface. This led to cyclic dynamic shear deformation of the tissue under investigation. After switching back to z.one™ internal mode, a second B-mode image was acquired. Comparing the internal B-mode images obtained before and after palpation provided a check for out-of-plane motion during palpation. This information was needed to exclude out-of-plane motion as a mechanism for clutter decorrelation, as explained below. Care was therefore taken during scanning to minimize out-of-plane motion.

2.4 Motion Tracking

Motion tracking for characterizing the tissue deformation produced by palpation, and its subsequent use for compensating for the deformation in photoacoustic images, was based on the PA-echo image sequence. Accuracy of motion tracking strongly depends on image quality. For ultrasound elastography, tracking is typically based on local block-matching between rigid template and search windows, optimizing a matching criterion (e.g., correlation).[35–38] The template window size must be chosen large enough to obtain a statistically significant correlation maximum. On the other hand, with a large window size, dilatation and shear deformation degrade the correlation between rigid windows. With the poor quality of the PA-echo images (see results), rigid-window block matching proved ineffective for motion tracking. Even a deformable mesh approach[39,40] yielded insufficiently stable results, due to strong decorrelation from image to image. Therefore tracking had to be based on a

more statistical approach, where the evolution of the PA-echo image over the whole sequence had to be taken into account.

The human eye is well adapted for performing such an analysis and can track pronounced features throughout the image sequence even if they are for part of the time obstructed by noise. Given the proof-of-principle nature of the present study, tracking was therefore carried out by eye, with the aid of an interactive user interface (written in Matlab™) which allowed trajectories to be assigned to sparsely distributed features throughout the image sequence. A model for displacement versus depth was then fitted to the collection of trajectories, assuming the lateral displacement to be a smooth function of depth. This method yielded stable motion tracking even in the presence of severe clutter, albeit with limited accuracy due to the simplified displacement model and trajectory identification errors.

2.5 Deformation Compensation

The lateral displacement $\Delta x_n(x, z)$ of an image element relative to its pre-deformation position (x, z) as a function of frame index n was used for deformation compensation of the PA images, where x is the lateral dimension and z is axial dimension (depth) of the image plane. Displacement was assumed to occur entirely parallel to the image plane, such that tissue deformation at frame index n could be modeled as a two-dimensional coordinate transformation $(x_n, z_n) = [x + \Delta x_n(x, z), z]$, where x_n and z_n are the coordinates of the image element in the nth frame. Deformation compensation of the PA image at index n was performed by inverting this coordinate transformation based on spatial interpolation. Because of the limited accuracy of the tracking method, an incoherent averaging approach was adopted by applying DCA to the envelope data as opposed to the radio frequency (RF) data. If RF echo-data were to be employed, and if tracking and compensation were not able to reregister correlated signals to within a fraction of the RF phase, this would on the one hand falsify the correlation analysis for clutter identification, and on the other hand result in loss of signal in the DCA images due to phase cancellation. Although coherent averaging of deformation-compensated RF signals may have been more efficient in cancelling the clutter, the use of incoherent averaging was considered an acceptable limitation, given the proof-of-principle character of the present study.

2.6 Clutter Analysis

Clutter identification and clutter analysis were based on time-lag correlation of the deformation-compensated photoacoustic (DC-PA) image sequence. The time-lag correlation $C_A(n, n + k)$ of an image region A in average-adjusted DC-PA images u_n and u_{n+k} obtained at time indices n and $n + k$ (with time lag k) was defined as:

$$C_A(n, n+k) = \frac{\int_A \mathrm{d}x\mathrm{d}z u_n(x, z)u_{n+k}(x, z)}{[\int_A \mathrm{d}x\mathrm{d}z u_n(x, z)^2 \cdot \int_A \mathrm{d}x\mathrm{d}z u_{n+k}(x, z)^2]^{1/2}}.$$

$$(1)$$

In a DC-PA sequence without clutter and noise, C_A is expected to be one, independent of the reference index n within the palpation scan and the lag k, as true PA sources remain at a constant position within the DC-PA sequence. With uncorrelated noise added, C shows a dip from lag $k = 0$ to $k = 1$, but is still constant for larger k. Clutter on the other hand is expected to

manifest as continuous decay of C_A for growing k, due to clutter decorrelation. Analysis of the time-lag autocorrelation thus provides a means to assess noise level, clutter level and the level of true PA signal within an image region of interest. Further evidence for clutter is the observed relationship between the decorrelation time constant and the displacement rate. Although decorrelation could also occur with speckle reformation upon the spatial rearrangement of subresolution PA sources, this kind of effect would depend on the shear rate as opposed to the displacement rate. In order to further analyze whether decorrelation was dependent on tissue shear deformation, the decorrelation rate was calculated as a function of the reference frame index n by fitting an exponential function to the time-lag autocorrelation function.

2.7 Deformation-Compensated Averaging

Clutter reduction is obtained by applying a moving temporal average to the DC-PA sequence. Signals originating from optical absorbers located in the image plane persist throughout the DC-PA sequence, and are therefore not affected by averaging. Averaging of decorrelating clutter on the other hand reduces the clutter level, and thus improves contrast-to-clutter ratio (CCR), the ratio of the difference between two photoacoustic signal levels and the mean clutter level, which is a measure of image contrast resolution. The impact of DCA on CCR depends on both the clutter decorrelation rate and the averaging-window length. The potential gain in CCR is expected to be roughly the square root of the number of uncorrelated measurements, or the ratio of averaging-window length and decorrelation time constant. The averaging length is limited by the maximum probe displacement and the amount of out-of-plane motion. In our experiments, out-of-plane motion was assessed via high quality ultrasound B-scans acquired at the start and the end of the scanning procedure. This permitted the exclusion of out-of-plane motion as an explanation for clutter decorrelation (see discussion). It was not, however, sufficient to quantify slight out-of-plane motion, which occurs over a large number of frames and limits DCA performance owing to decorrelation of true signal. A fixed averaging length of 20 frames was therefore chosen, based on trial and error, as a value that yielded good CCR gain for all scans. The potential CCR improvement was calculated as the square root of the ratio of this averaging length and the clutter decorrelation rate. Assessing the true resulting contrast-resolution improvement by methods other than by eye has proven a challenging task in *in vivo* scanning, where the true distribution of PA sources is not known. The final conclusions drawn in this preliminary study are therefore mostly based on the visual appearance of DCA results.

3 Results

All PA and PA-echo images in this paper show logarithmically compressed envelope data, and are grayscale coded with high signal amplitude in white. They are also compensated for depth-dependent signal variation, i.e., time-gain compensation, for ultrasound attenuation in the PA-echo images, and for both ultrasound attenuation and optical fluence distribution in the PA images.

3.1 Duplex Photoacoustic and Photoacoustic-Echo Imaging, and Motion Tracking

Figure 1 shows example duplex PA and PA-echo ultrasound images of the first author's neck in transaxial section close to
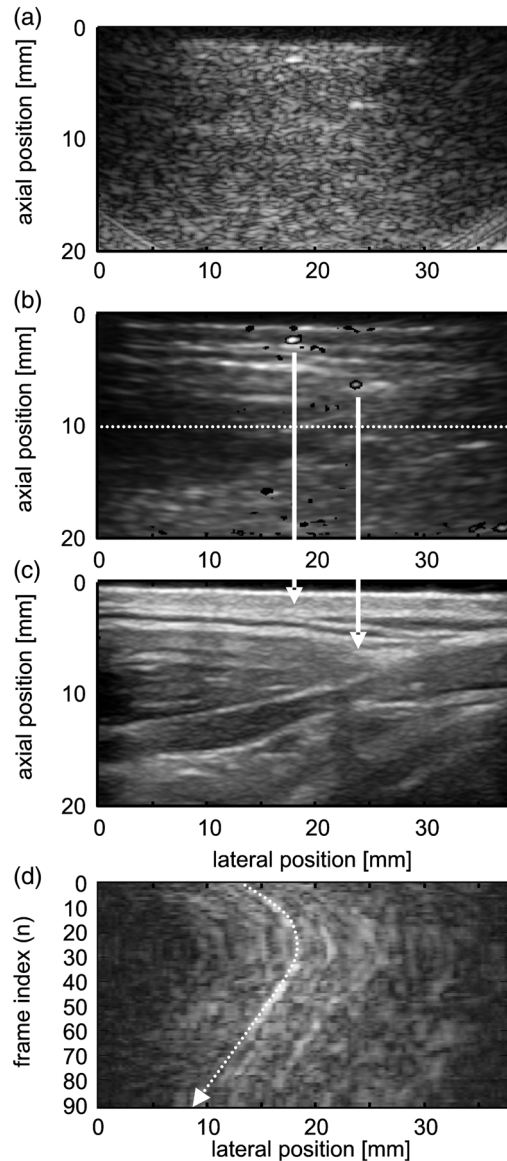
Fig. 1 (a) PA image, reconstructed from the PA part of the signal data. (b) Echo ultrasound image reconstructed from the PA-echo part of the signal data, overlaid with PA data after thresholding, to show only the highest amplitudes from (a). (c) The z.one™ internal B-mode image is shown. The similarity between the z.one™ image and the PA-echo image permits registration of PA features with the anatomical context shown in the z.one™ image (white arrows). (d) Example of manual motion tracking based on the PA-echo image sequence. A tissue trajectory (dotted arrow) is drawn on a constant-depth M-mode (CM mode) image, obtained at 10-mm depth indicated by the horizontal dotted line in (b).

the thyroid (at the position indicated in the pictorial diagram inset in Fig. 2). Figure 1(a) is the PA image reconstructed from the upper part of a frame of ultrasound signals, containing the PA data, and Fig. 1(b) is the echo ultrasound image reconstructed from the lower part of the same frame, containing PA-echo data. The PA-echo image is shown with an overlay of the PA image after thresholding to show only the signals with the highest amplitude from Fig. 1(a). This illustrates the registration between the PA image and the PA-echo image, which is inherent because the two images were generated with the same laser pulse. For comparison, Fig. 1(c) is the conventional pulse-echo image obtained with the internal B-mode facility of the
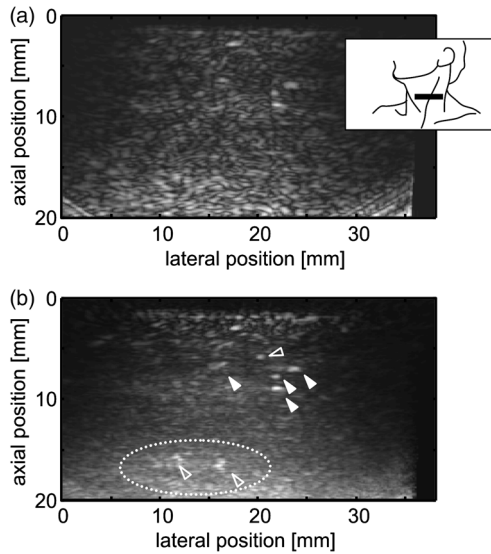
Fig. 2 PA image from the neck, (a) prior to DCA processing, and (b) post DCA. Full white arrows denote image features with clearer appearance after DCA, demonstrating contrast improvement. Empty white arrows denote features which are distinguished only after DCA, demonstrating both contrast improvement and increased imaging depth. The dashed oval encircles a region of generally improved contrast. [Inset in (a): black bar denotes the probe position.]

z.one™. The PA-echo images can therefore be used as an intermediate step for registering PA images with the conventional pulse-echo images, based on corresponding features such as those indicated by the white arrows in Fig. 1. In the present study, however, the PA-echo sequence was used for tracking tissue motion during the period of palpation. As explained above, the poor quality of the PA-echo images meant that motion tracking had to be performed visually using envelope data. For this purpose, trajectories such as that shown in Fig. 1(d) (white dotted line) were interactively chosen, each being drawn by eye on a constant-depth M-mode (CM-mode) image, as illustrated. CM-mode images at various depths were used and trajectories were drawn starting at various lateral positions. The displacement model described above was then fitted to the collection of trajectories, which had a regularizing effect, reducing tracking errors. This gave what was believed to be a robust estimate of the displacement as a function of position and frame index, which could then be used to determine the deformation-compensation function that was to be applied to the PA image sequence.

3.2 *Image Analysis and Evidence for the Existence of Clutter*

Image analysis to demonstrate the presence or absence of clutter in various image regions was based on the time-lag correlation of the DC-PA sequence as defined in Eq. 1. Results are shown for the neck scan in Fig. 2, and for the forearm scan in Fig. 3. Analysis regions were chosen at locations where DCA processed scans suggested low level of true PA signal. One region was chosen at depth, where large tissue displacement relative to the skin surface was expected to result in strong clutter decorrelation [see Figs. 4(a) and 5(a), region *A*]. A second region was chosen close to the skin surface, where the rate of change of displacement was low, but the shear rate was large [Figs. 4(a) and 5(a), region *B*]. White overlays to the right of Figs. 4(a)
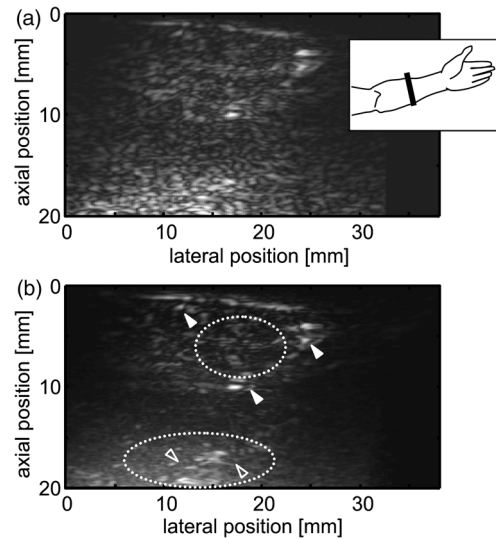
Fig. 3 Analogous to Fig. 2, but showing results from the left forearm.

and 5(a) show the lateral-displacement depth profile at the maximum probe displacement, which reaches a maximum of 5 and 8 mm displacement, respectively, at the largest depth where the shear rate appears to be low, and suggests a large shear rate close to the surface. Figures 4(b) and 5(b) show the displacements obtained at the depths of regions *A*, as a function of frame index, illustrating the oscillatory motions of the palpation. Figures 4(c) and 5(c) show the time-lag correlation functions $C(n, n + k)$ evaluated at frame indices n for both large and zero displacement rate [indicated in Figs. 4(b) and 5(b) by vertical lines], for the image regions *A*. Figures 4(d) and 5(d) show the time-lag correlation functions for the same frame indices, but for regions *B*. It may be seen that $C(k)$ strongly depends on the displacement rate. Zero displacement rate results in slow decorrelation [solid line in Figs. 4(c) and 5(c)]. After a small dip at lag $k = 1$, caused by uncorrelated noise, correlation stays fairly constant. This demonstrates a high level of systematic signal at zero displacement rate. A steady decrease in correlation for lags larger than five is related to growing displacement rate at those lags. In contrast, at maximum displacement rate, full decorrelation takes place even for small lags ($k <$ five) within region *A*. The interdependence between displacement rate and decorrelation is further substantiated in Figs. 4(b) and 5(b), where the decorrelation rate, defined as the slope of the exponential fit to the correlation function, is plotted together with the displacement curve. Decorrelation rate is smallest for zero displacement rate and largest for large displacement rates.

A possible explanation for decorrelation with tissue deformation could be out-of-plane motion of diffusely distributed PA sources. This would however require significant displacement perpendicular to the image plane, of around 2 mm (thickness of the image plane) per five displacement steps. However, the B-mode images acquired prior to and following the palpation scan indicated only small out-of-plane motion, around 2 mm over the whole 90-frame scan sequence, i.e., about 0.1 mm per five displacement steps. Out-of-plane motion can therefore be excluded as an explanation for decorrelation. A further possible explanation for decorrelation is speckle reformation associated with the spatial rearrangement of subresolution photoacoustic
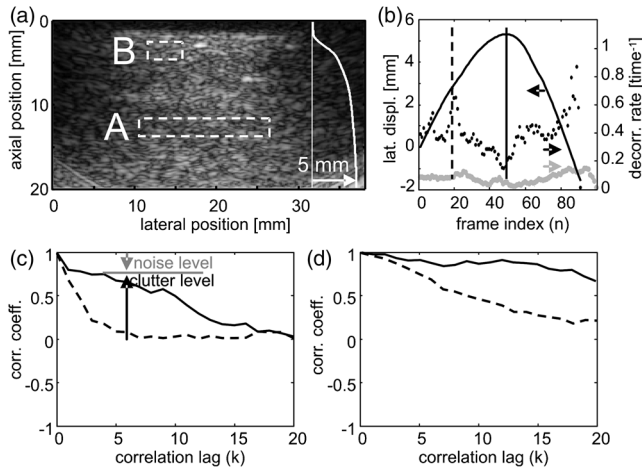
Fig. 4 Image statistics for the neck scan. (a) PA image with windows for correlation analysis (white dashed rectangles, *A* and *B*) and a depth profile of the maximum lateral displacement (white vertical line, and vertical graph, to the right). (b) Displacement at the depth of region *A* (solid graph, arrow points to left scale), decorrelation rate in window *A* and window *B* as function of frame index *n* (black and grey dots, respectively, arrows point to right scale). (c) Time-lag correlation graphs for window *A*, for zero displacement rate (solid line), starting at the time indicated in (b) (solid vertical line), and for rapid displacement (dashed line), starting at the time indicated in (b) (dashed vertical line). At zero displacement rate, a small dip from $k = 0$ to $k = 1$ indicates stochastic noise (gray arrow), while after that, correlation persists up to about $k = 10$, suggesting systematic signal. In contrast, with rapid displacement, decorrelation is much faster. The spacing between the dotted and the solid line indicates that clutter is present (black arrow). (d) Same as in (c), but for window *B*. Decorrelation is slower owing to slower displacement close to the skin surface.

Fig. 5 Image statistics for the forearm. (a), (b), (c), and (d) analogous to Fig. 3.

sources upon tissue shear. This effect would be proportional to the shear rate[41] as opposed to the displacement rate. However, the time-lag correlation evaluated in region *B*, where the shear rate was large, indicates very slow decorrelation [Figs. 4(d) and 5(d)], compared to region *A* where the shear rate was low. The evidence collected therefore strongly supports the hypothesis that clutter was present in the clinical scans.

3.3 *Deformation-Compensated Averaging*

For DCA, a moving temporal average was applied to the DC-PA sequence, with window length spanning 20 frames, or 2-s scan time. This interval length was chosen as a compromise between contrast improvement and blurring. Due to inaccurate motion tracking, blurring of real PA features over long time intervals could not be avoided. In addition, out-of-plane motion, while not sufficient to explain short-time decorrelation of the diffuse PA background, still affected the persistence of PA structures on longer time scales. A moving average over 20 frames yielded good results with all scans.

Figures 2 and 3 illustrate the effect of DCA on the two PA image sequences acquired during palpation. They illustrate that DCA improves contrast resolution in the clinical scans. This is mainly noticed around some high amplitude features already visible prior to DCA. DCA led to a more pronounced appearance of these features, and a smoothing of speckled PA background leading to a cleaner appearance of their vicinity (full white arrows). In addition, however, there were features made visible at depth which were not visible prior to DCA (empty white arrows). This indicates that DCA not only improved

contrast resolution, but also led to increased imaging depth. Indeed, it can be seen in Figs. 2 and 3 that there is a pronounced increase in the clutter-reducing effect of DCA for depths greater than about 8 mm.

The contrast-resolution improvement is in agreement with the theoretical expectation described above. Based on the averaging length of 20 frames and a decorrelation rate of 0.5 per frame (taken from Figs. 4 and 5), the maximum potential CCR improvement was expected to be three (the square root of the product of averaging length and clutter-decorrelation rate). Quantitatively assessing the achieved CCR improvement was however challenging, because the "true" spatial distribution of PA sources was not known.

4 Discussion

For the first time, the existence of clutter in clinical epiphotoacoustic scans has been demonstrated. This was based on time-lag autocorrelation analysis in conjunction with scanning during tissue deformation induced by palpation with the probe, a method that appears to be a valuable tool for differentiating between random noise, clutter and true PA signal. This approach may in future be suitable for identifying and quantifying clutter in a thorough clinical study, in order to investigate the influence of tissue type, and in particular components such as skin melanin content and vascularity, on epiphotoacoustic image contrast. The same approach also holds potential for identifying whether clutter exists in small animal imaging. Clutter identification is very important as, until now, PA images have been interpreted without verifying the true origin of displayed signals, which might often lead to false conclusions. Because a commercial duplex (epi-) photoacoustic and pulse-echo system is now available for small-animal imaging, our results are of potential importance for the preclinical imaging research community.

This is also the first demonstration that deformation-compensated averaging is a valuable method for clutter reduction, not only in simulations and phantom experiments, but also in clinical PA imaging. Despite the limitations of the preliminary duplex imaging method developed (discussed below), we were able to achieve significant contrast-resolution improvement using DCA with freehand scanning during palpation with the probe, a technique that is already in widespread clinical use to generate images related to tissue elasticity. This demonstrates

the practical suitability of this method for integration with conventional ultrasound clinical imaging procedures. It could also take advantage of real-time motion tracking, which is readily available with ultrasound scanners featuring quasi-static elastography.[42] Motion compensation in turn is computationally very cheap; thus DCA PA imaging could be presented in real time, providing feedback on the outcome of palpation for interactive adjustment of the probe guidance for optimum result. The results of the present study therefore represent a promising starting point for much further development.

The above results were made possible by the use of PA-echo imaging, which allowed real-time duplex data acquisition and thus freehand clinical scanning during tissue deformation, and proved to be a valuable tool for deformation characterization and compensation of photoacoustic images. Unfortunately the photoacoustic-echo method provided much lower quality images than conventional pulse-echo methods that use transmit-wave focusing, and its use limited the motion-tracking accuracy that could be achieved. This in turn restricted clutter analysis and DCA to envelope data. A further potential limitation to the photoacoustic-echo method was the dependence of the echo amplitude on the intensity of the backscattered light. Variation of the transmit-wave amplitude due to fluctuations in the backscattered light with transducer motion was in principle possible. However, ultrasound displacement tracking did not depend on the absolute pulse-echo amplitude, and thus the presented PA clutter analysis and DCA results were not influenced by fluctuations of the backscattered light. Nevertheless, future work on DCA would be worthwhile, using real-time duplex interleaved epiphotoacoustic and high quality conventional pulse-echo scanning, which can be expected to allow the use of RF data and to further increase the epiphotoacoustic contrast resolution and maximum imaging depth.

Research that has explored applications of approaches similar to DCA (but with different objectives) is found in echo ultrasound imaging. In strain compounding, which was proposed by Li et al. for speckle reduction[41], the same principle (motion tracking, motion compensation, averaging) was applied to the pulse-echo envelope data. The positive impact of strain compounding on image contrast was explained by speckle decorrelation upon tissue deformation, due to spatial rearrangement of acoustic scatterers inside the resolution cell. However, ultrasound speckle decorrelation with shear deformation is slow compared with clutter decorrelation. Therefore perhaps the positive effect on contrast observed by Li et al. could have been partially explained by clutter reduction, as well as speckle reduction.

In a further approach related to DCA, principal-component analysis, was used for eliminating acoustic reverberations from the abdominal wall in echo ultrasound.[43] In images obtained during palpation to create a uniaxial compressive load, abdominal wall clutter remains relatively stationary and can thus be identified as the first principal component of the image sequence against the motion of underlying tissue structures. The first principal component is then removed, leaving a clutter-reduced image. The success of this approach depends on correlated clutter over time. A similar approach was investigated for PA imaging together with DCA by Jaeger et al.[24] Performance in PA imaging, however, is typically limited by rapid clutter decorrelation, because much PA clutter arises from incoherent random PA sources rather than from a single spatially coherent source as in the case of abdominal-wall pulse-echo clutter.

DCA for clutter reduction and strain compounding has applications beyond PA imaging and echo ultrasound, for example in optical coherence tomography (OCT). If imaging depth and contrast resolution in OCT is limited to the regime where single scattering prevails, DCA may assist in improving performance. Due to the much larger ratio of coherence length to wavelength in OCT, as compared to ultrasound, rapid speckle decorrelation with tissue deformation is expected and a first main impact of strain compounding on contrast may well occur by reducing speckle. However speckle reduction by itself does not alter imaging depth. DCA opens a different perspective, that multiple scattering clutter in OCT could be reduced, extending imaging depth beyond the single-scattering regime as well as improving contrast resolution.

5 Conclusion

An investigation of clutter in epi-mode clinical photoacoustic scanning, based on freehand and real-time acquisition of duplex photoacoustic and photoacoustic-echo scans of the neck and forearm, has provided evidence that much of the speckled pattern typical for clinical photoacoustic imaging is related to clutter, rather than optical absorption in the imaging plane. Using deformation-compensated averaging of epiphotoacoustic images acquired during palpation to induce a shear deformation of the tissue, clutter was substantially reduced and thus contrast resolution and imaging depth improved. These findings are highly relevant for clinical photoacoustic imaging, where implementation as an additional component of freehand diagnostic ultrasound technology is a desirable goal and a large imaging depth is required, but the method might also hold promise for improving images from echo ultrasound, optical coherence tomography and other modalities.

References

1. M. Xu and L. V. Wang, "Photoacoustic imaging in biomedicine," *Rev. Sci. Instrum.* **77**(4), 41101 (2006).
2. K. P. Köstli et al., "Optoacoustic imaging using a three-dimensional reconstruction algorithm," *IEEE J. Sel. Top. Quant. Electron.* **7**(6), 918–23 (2001).
3. Y. Xu, D. Feng, and L. V. Wang, "Exact frequency-domain reconstruction for thermoacoustic tomography. I. Planar geometry," *IEEE Trans. Med. Imag.* **21**(7), 823–828 (2002).
4. M. Xu and L. V. Wang, "Universal back-projection algorithm for photoacoustic computed tomography," *Phys. Rev. E Stat. Nonlinear Soft Matter Phys.* **71**(1), 016706 (2005).
5. M. Jaeger et al., "Fourier reconstruction in optoacoustic imaging using truncated regularized inverse *k*-space interpolation," *Inverse Probl.* **23**(6), S51–S63 (2007).
6. X. Wang et al., "Noninvasive imaging of hemoglobin concentration and oxygenation in the rat brain using high-resolution photoacoustic tomography," *J. Biomed. Opt.* **11**(2), 024015 (2006).
7. H. F. Zhang et al., "Functional photoacoustic microscopy for high-resolution and noninvasive in vivo imaging," *Nat. Biotechnol.* **24**(7), 848–851 (2006).
8. S. Hu and L. V. Wang, "Photoacoustic imaging and characterization of the microvasculature," *J. Biomed. Opt.* **15**(1), 011101 (2010).
9. J. Laufer et al., "Quantitative spatially resolved measurement of tissue chromophore concentrations using photoacoustic spectroscopy: application to the measurement of blood oxygenation and haemoglobin concentration," *Phys. Med. Biol.* **52**(1), 141–168 (2007).

10. B. Wang et al., "Plasmonic intravascular photoacoustic imaging for detection of macrophages in atherosclerotic plaques," *Nano Lett.* **9**(6), 2212–2217 (2009).
11. Y. Wang et al., "Photoacoustic tomography of a nanoshell contrast agent in the in vivo rat brain," *Nano Lett.* **4**(9), 1689–1692 (2004).
12. X. D. Wang et al., "Noninvasive photoacoustic angiography of animal brains in vivo with near-infrared light and an optical contrast agent," *Opt. Lett.* **29**(7), 730–732 (2004).
13. D. P. J. Pan et al., "Near infrared photoacoustic detection of sentinel lymph nodes with gold nanobeacons," *Biomat.* **31**(14), 4088–4093 (2010).
14. D. R. McCormack et al., "Enhanced photoacoustic detection of melanoma cells using gold nanoparticles," *Lasers Surg. Med.* **43**(4), 333–338 (2011).
15. C. L. Bayer et al., "Molecular diagnosis of cancer using multiplex photoacoustic imaging with targeted nanorods," *Ultrasonics Symposium*, San Diego, IEEE, Piscataway, pp. 503–506 (11–14 Oct. 2010).978-1-4577-0382-9
16. S. A. Ermilov et al., "Laser optoacoustic imaging system for detection of breast cancer," *J. Biomed. Opt.* **14**(2), 024007 (2009).
17. S. Manohar et al., "Initial results of in vivo non-invasive cancer imaging in the human breast using near-infrared photoacoustics," *Opt. Express* **15**(19), 12277–12285 (2007).
18. D. R. Bauer et al., "3-D photoacoustic and pulse echo imaging of prostate tumor progression in the mouse window chamber," *J. Biomed. Opt.* **16**(2) (2011).
19. Y. Junjie et al., "Label-free oxygen-metabolic photoacoustic microscopy *in vivo*," *J. Biomed. Opt.* **16**(7), 076003 (2011).
20. J. J. Niederhauser et al., "Combined ultrasound and optoacoustic system for real-time high-contrast vascular imaging in vivo," *IEEE Trans. Med. Imag.* **24**(4), 436–440 (2005).
21. A. Aguirre et al., "Coregistered three-dimensional ultrasound and photoacoustic imaging system for ovarian tissue characterization," *J. Biomed. Opt.* **14**(5), 054014 (2009).
22. R. G. M. Kolkman et al., "Real-time in vivo photoacoustic and ultrasound imaging," *J. Biomed. Opt.* **13**(5), 050510 (2008).
23. R. J. Zemp et al., "Photoacoustic imaging of the microvasculature with a high-frequency ultrasound array transducer," *J. Biomed. Opt.* **12**(1), 010501 (2007).
24. M. Jaeger et al., "Reduction of background in optoacoustic image sequences obtained under tissue deformation," *J. Biomed. Opt.* **14**(5), 054011 (2009).
25. S. A. Ermilov et al., "Real-time optoacoustic imaging of breast cancer using an interleaved two-laser imaging system coregistered with ultrasound," *Proc. SPIE* **7564**, 75641W (2010).
26. I. M. Graf et al., "Methodical study on plaque characterization using integrated vascular ultrasound, strain and spectroscopic photoacoustic imaging," *Proc. SPIE* **7899**, 789902 (2011).
27. B. Wang et al., "Detection of lipid in atherosclerotic vessels using ultrasound-guided spectroscopic intravascular photoacoustic imaging," *Opt. Express* **18**(5), 4889–4897 (2010).
28. B. Wang et al., "Intravascular photoacoustic imaging," *IEEE J. Sel. Topics Quantum Electron.* **16**(3), 588–599 (2010).
29. J. C. Bamber, "Acoustical characteristics of biological media," in *Encyclopedia of Acoustics*, M. J. Crocker, Ed., John Wiley, New York, pp. 1703–1726 (1997).
30. T. D. Khokhlova et al., "Optoacoustic imaging of absorbing objects in a turbid medium: ultimate sensitivity and application to breast cancer diagnostics," *Appl. Opt.* **46**(2), 262–272 (2007).
31. Z. Xie et al., "Photoacoustic imaging of deep targets in the breast using a multichannel 2D array tranducer," *Proc. SPIE* **7899**, 789907 (2011).
32. M. Jaeger et al., "Improved contrast deep optoacoustic imaging using displacement-compensated averaging: breast tumour phantom studies," *Phys. Med. Biol.* **56**(18), 5889–5901 (2011).
33. M. Jaeger et al., "Clinical feasibility of duplex photoacoustic and ultrasound pulse-echo imaging using photoacoustic transmit pulses," *Ultrasound Med. Biol.* (submitted).
34. M. Jaeger, M. Frenz, and D. Schweizer, "Iterative reconstruction algorithm for reduction of echo background in optoacoustic images," *Proc. SPIE* **6856**, 68561C (2008).
35. M. ODonnell et al., "Internal displacement and strain imaging using ultrasonic speckle tracking," *IEEE Trans. Ultrason., Ferroelectr., Freq. Control* **41**(3), 314–325 (1994).
36. J. Ophir et al., "Elastography—a quantitative method for imaging the elasticity of biological tissues," *Ultrason. Imaging* **13**(2), 111–134 (1991).
37. T. Shiina et al., "Real time tissue elasticity imaging using the combined autocorrelation method," *J. Med. Ultrason.* **26**(2), 57–66 (2002).
38. M. M. Doyley et al., "A freehand elastographic imaging approach for clinical breast imaging: system development and performance evaluation," *Ultrasound Med. Biol.* **27**(10), 1347–1357 (2001).
39. Y. N. Zhu, P. Chaturvedi, and M. F. Insana, "Strain imaging with a deformable mesh," *Ultrason. Imag.* **21**(2), 127–146 (1999).
40. F. Yeung et al., "Feature-adaptive motion tracking of ultrasound image sequences using a deformable mesh," *IEEE Trans. Med. Imag.* **17**(6), 945–956 (1998).
41. P.-C. Li and M.-J. Chen, "Strain compounding: a new approach for speckle reduction," *IEEE Trans. Ultrason. Ferroelectrics Freq. Contr.* **49**(1), 39–46 (2002).
42. A. Thomas et al., "Real-time elastography—an advanced method of ultrasound: first results in 108 patients with breast lesions," *Ultrasound Obst. Gyn.* **28**(3), 335–340 (2006).
43. M. A. Lediju et al., "A motion-based approach to abdominal clutter reduction," *IEEE Trans. Ultrason. Ferroelectrics Freq. Contr.* **56**(11), 2437–2449 (2009).